Near-field Effects on Cathodoluminescence Outcoupling in Perovskite Thin Films

– SUPPLEMENTARY INFORMATION –

R. Schot*,[1] I. Schuringa*,[1] A. Rodríguez Echarri,[1] L. Sonneveld,[1]
T. Veeken,[1] Y. Lu,[2] S. Stranks,[2] A. Polman,[1] B. Ehrler,[1] and S. Fiedler[1]
[1] *LMPV-Sustainable Energy Materials Department, AMOLF,*
Science Park 104, 1098 XG Amsterdam, The Netherlands
[2] *Department of Chemical Engineering and Biotechnology,*
University of Cambridge, Philippa Fawcett Drive, Cambridge CB3 0AS, U.K.

The supplementary information contains further figures complementing the discussion in the main text. Additional experimental data is shown, such as X-ray diffractograms, line traces, a 5 keV map of the large grain sample, SEM crosscuts, and luminescence lifetime measurements. We also devoted a chapter to the effect of the non-radiative decay rate on the simulated line traces. Moreover, we present further derivations of the calculations and analytics used in a simplified one-dimensional problem. In particular, we consider that a set of dipoles is placed within an infinite parallel plate radiating to the far field. Additionally, their emission is weighted by the excitation profile provided by the incident electrons characterized by the energy deposited while penetrating the perovskite via Monte Carlo simulations.

CONTENTS

S1. X-RAY DIFFRACTOGRAM

Figure S1 shows the X-ray diffractogram for the perovskite films on silicon, before annealing (blue) and after annealing for 30 minutes at 200 °C (orange). The orthorhombic $CsPbBr_3$ phase is indicated with green squares, and the $CsPb_2Br_5$ phase with red circles. The appearance of the $CsPb_2Br_5$ phase could explain the optically inactive grains, which are visible in Figure 1 in the main text [1], [2], [3].

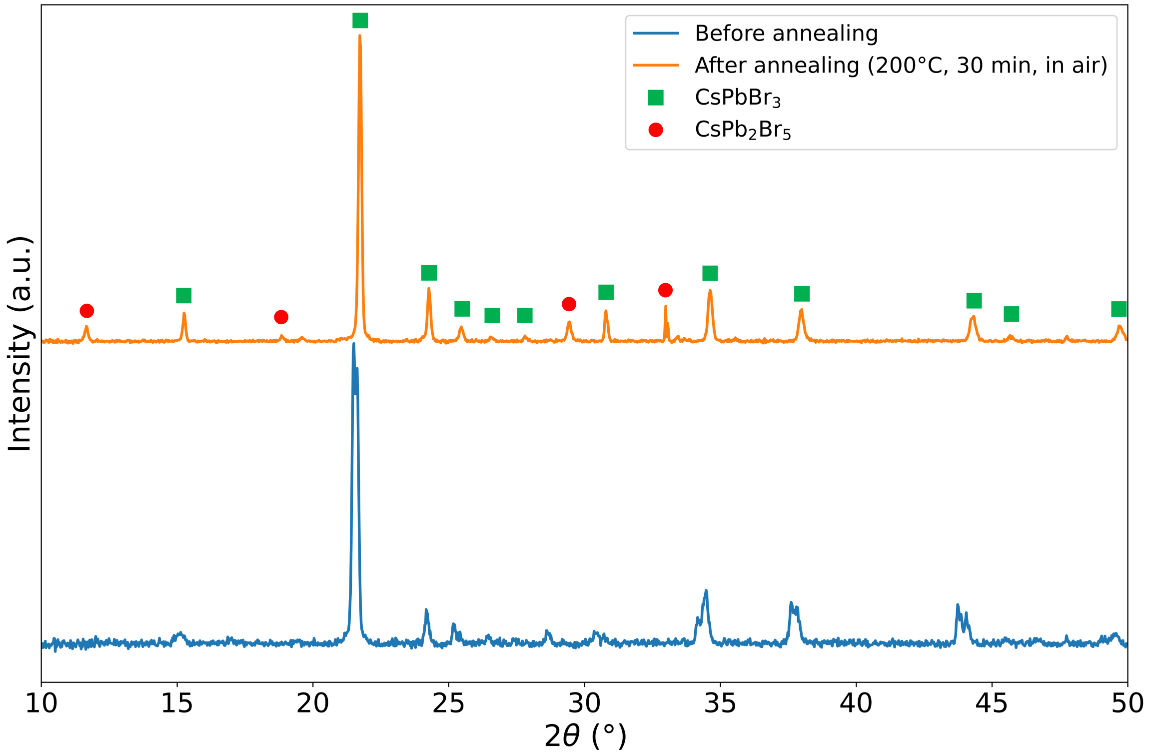

FIG. S1. X-ray diffractogram (XRD) for the perovskite films on silicon, before (blue) and after annealing (orange). The orthorhombic $CsPbBr_3$ phase is indicated with green squares, and the $CsPb_2Br_5$ phase with red circles.

S2. 2 keV AND 5 keV AFM/CL LINE TRACES FOR THE SMALL-GRAIN SAMPLES

The atomic force microscopy (AFM) and cathodoluminescence (CL) line traces for both 5 keV and 2 keV incident electrons are shown in Figure S2. The simulations belonging to the traces are shown in Figure 2 in the main text.

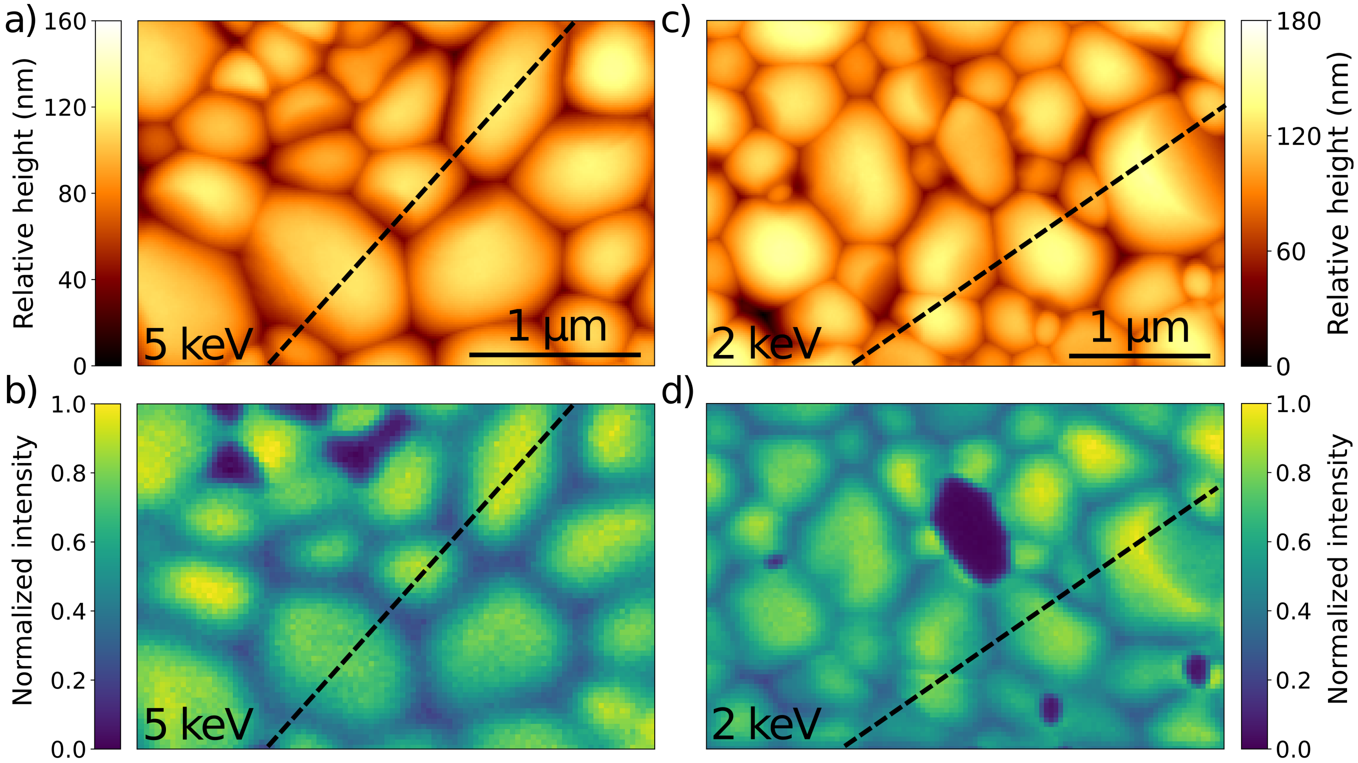

FIG. S2. AFM and CL line traces for (a,b) 5 keV and (c,d) 2 keV incident electrons, indicated with a dashed black line. The scalebar in the AFM maps applies to both the AFM and CL map.

S3. PEROVSKITE THICKNESS MEASUREMENTS

The silicon substrate depth was calculated by subtracting the average perovskite grain thickness from the average relative grain height measured with AFM. The grain thickness was obtained from cross-sectional SEM measurements on cleaved samples, shown in Figure S3(d,e). The AFM average peak height was determined numerically by locating points where the derivative of the surface profile equaled zero. To exclude grains growing on top of other grains, a maximum height threshold of 130 nm (for the 5 keV map) and 160 nm (for the 2 keV map) was applied. These substantially higher grains are particularly evident in Figure S3(b). For the 2 and 5 keV small-grain simulations, the two AFM maps were analyzed separately, while the same set of crosscut measurements were used. Figures S3(a,b) show AFM maps with the identified peaks, along with cross sections for the small- and large-grain simulations in (d,e).

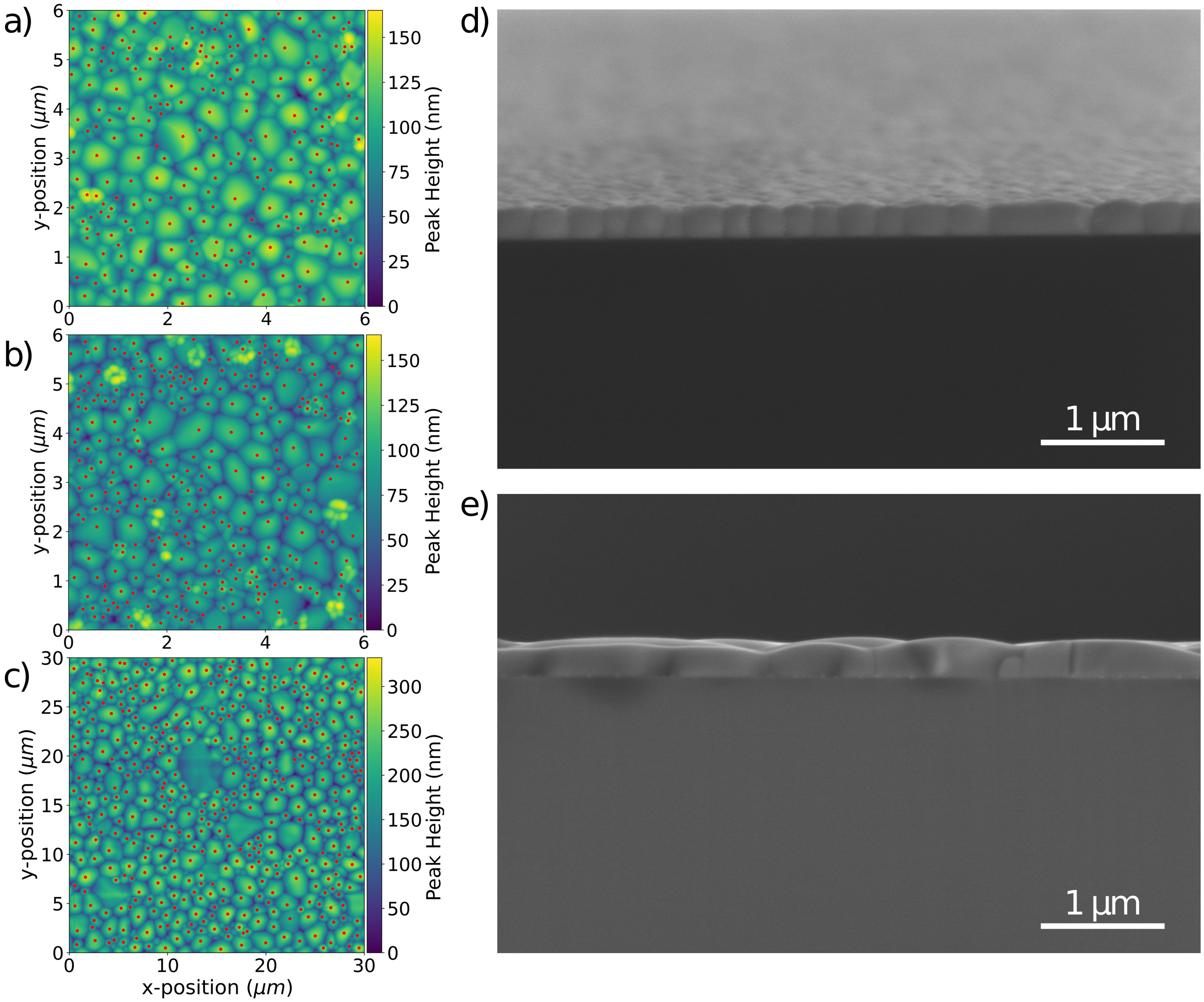

FIG. S3. AFM maps for (a) 2 keV small-grain, (b) 5 keV small-grain, and (c) 2 keV large-grain samples. Red dots indicate numerically calculated grain peak positions, where the derivative of the surface profile equaled zero. SEM crosscuts for (d) small-grain and (e) large-grain samples. Note the difference in x- and y-scales between (a,b) and (c)

S4. 5 keV MEASUREMENT ON LARGE-GRAIN FILM

A 5 keV CL map of the same film as the 2 keV map in Figure 3(a) is shown in Figure S4. Compared with the 2 keV map, the rings are less clearly visible, which is due to the larger excitation volume of the 5 keV electrons, as described in the main text.

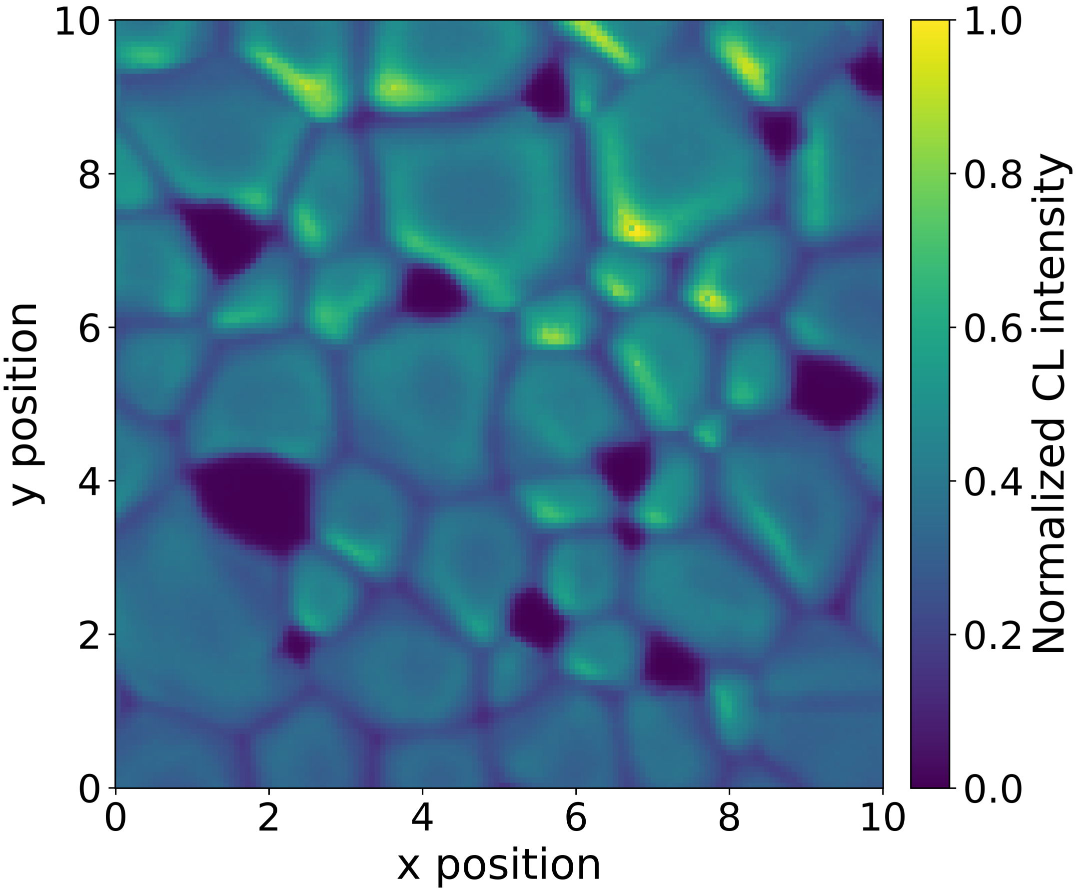

FIG. S4. Experimental CL map (5 keV, λ=525 nm, 6 nm bandwidth) for a $CsPbBr_3$ film with grain sizes ranging from roughly 1 to 4 µm.

S5. THE EFFECT OF THE NON-RADIATIVE DECAY RATE

The spontaneous emission rate of an optical emitter is governed by the local optical density of states (LDOS), that reflects the density of optical modes to which the emitter can couple. Following the pioneering work of Drexhage [4] several experiments have demonstrated how the variation of the LDOS near an interface [5] or across a thin film [6], [7] results in a depth-dependent radiative rate of embedded emitters. The modification of the LDOS is often expressed in terms of the Purcell factor $F_p(\mathbf{r})$, which quantifies the enhancement or suppression of the radiative decay rate relative to that in a homogeneous reference medium. In the case of a non-unity internal quantum efficiency (IQE), variations in the LDOS lead to corresponding changes in the Purcell factor, thereby modulating the luminescence intensity. Under steady-state excitation in the linear pump regime (i.e. not in saturation), which is common for CL and PL experiments, the position dependent intensity is given by

$$\mathrm{I}(\mathbf{r}) = \eta_{\text{out}}(\mathbf{r})\,\frac{\Gamma_r(\mathbf{r})}{\Gamma_r(\mathbf{r}) + \Gamma_{nr}(\mathbf{r})} = \eta_{\text{out}}(\mathbf{r})\,\frac{F_p(\mathbf{r})\,\Gamma_{r,0}}{F_p(\mathbf{r})\,\Gamma_{r,0} + \Gamma_{nr}(\mathbf{r})} \tag{1}$$

with η_{out} the outcoupling efficiency, $\Gamma_r(\mathbf{r})$ the radiative decay rate, $\Gamma_{nr}(\mathbf{r})$ the non-radiative decay rate, $F_p(\mathbf{r})$ the Purcell factor, and $\Gamma_{r,0}$ the radiative decay rate of the dipole in a homogeneous reference medium. In the limit of $\Gamma_r(\mathbf{r}) \gg \Gamma_{nr}(\mathbf{r})$ (IQE $= 1$), this equation reduces to

$$\mathrm{I}(\mathbf{r}) \approx \eta_{\text{out}}(\mathbf{r})\,\frac{\Gamma_r(\mathbf{r})}{\Gamma_r(\mathbf{r})} = \eta_{\text{out}}(\mathbf{r}) \tag{2}$$

so the collected CL or PL does not depend on the Purcell factor. In the limit of $\Gamma_r(\mathbf{r}) \ll \Gamma_{nr}(\mathbf{r})$ (IQE $\ll 1$), equation 1 can be written as

$$\mathrm{I}(\mathbf{r}) \approx \eta_{\text{out}}(\mathbf{r})\,\frac{\Gamma_r(\mathbf{r})}{\Gamma_{nr}(\mathbf{r})} = \eta_{\text{out}}(\mathbf{r})\,F_p(\mathbf{r})\,\frac{\Gamma_{r,0}}{\Gamma_{nr}(\mathbf{r})}. \tag{3}$$

If we assume that the non-radiative decay rate is constant throughout the film, we can write

$$\mathrm{I}(\mathbf{r}) \propto \eta_{\text{out}}(\mathbf{r})\,F_p(\mathbf{r}), \tag{4}$$

which indicates that the CL or PL intensity is directly proportional to the Purcell factor in the non-radiative regime. To investigate how the simulated CL line traces would behave in this regime, we multiplied every dipole's far field intensity with its Purcell factor, and compared the resulting line traces with the ones simulated in the purely radiative regime (IQE $= 1$). The obtained 5 keV and 2 keV line traces for the small grain samples, together with the Purcell factors, are shown in Figures S5 and S6 respectively. It can be seen that the effect of the Purcell factor multiplication is negligible, indicating that variations in outcoupling efficiency are the dominant contribution to the line trace.

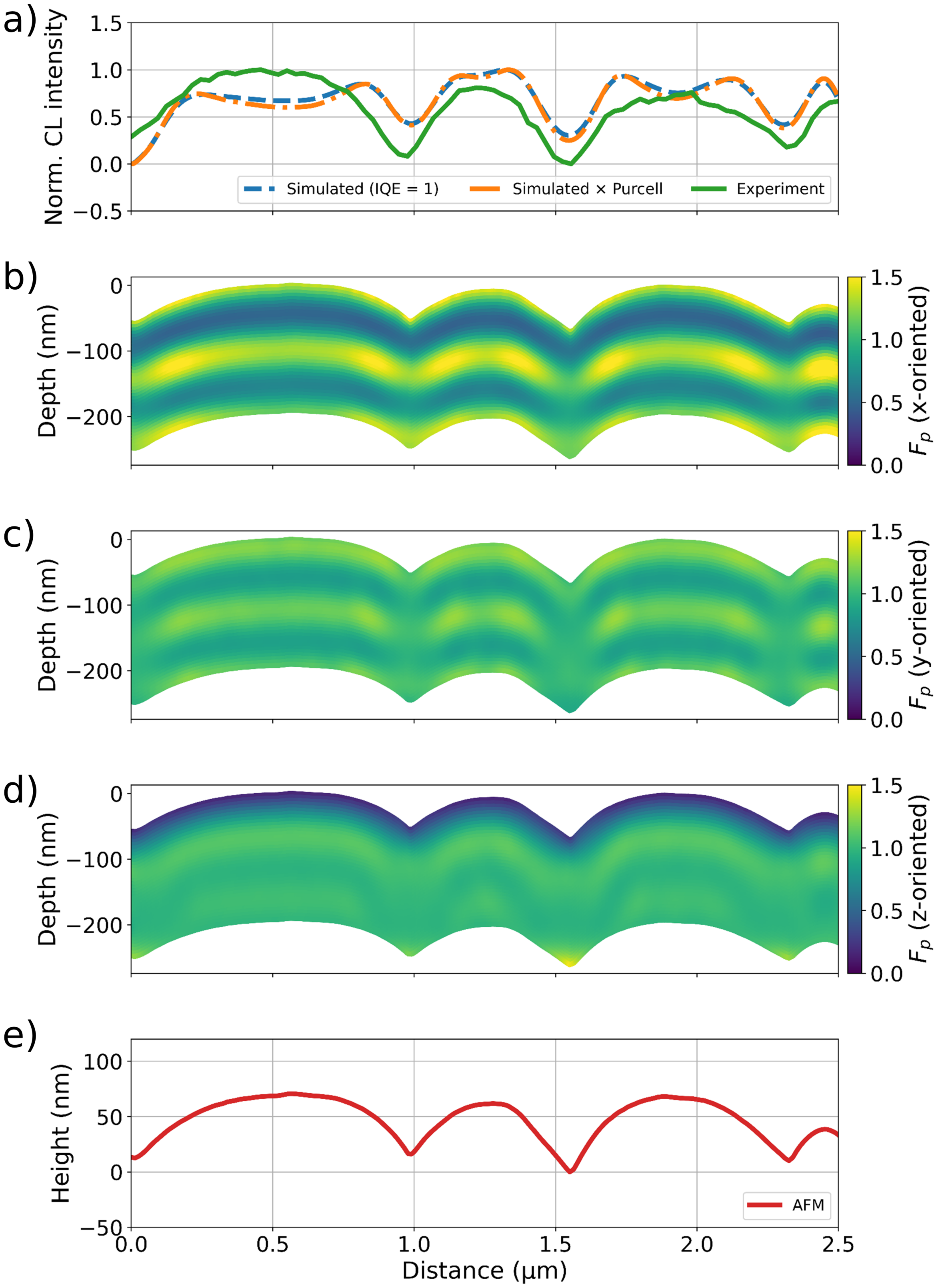

FIG. S5. (a) Experimental CL line trace (5 keV, $\lambda = 525$ nm, 6 nm bandwidth) (green) together with the simulated line traces with IQE = 1 (blue dashed line) and with IQE $\ll$ 1 (dashed orange line). (b,c,d) Simulated Purcell factors as a function of position for the same geometry as in Figure 3 (b) in the main text. (e) AFM line trace that was used as an input in the simulations.

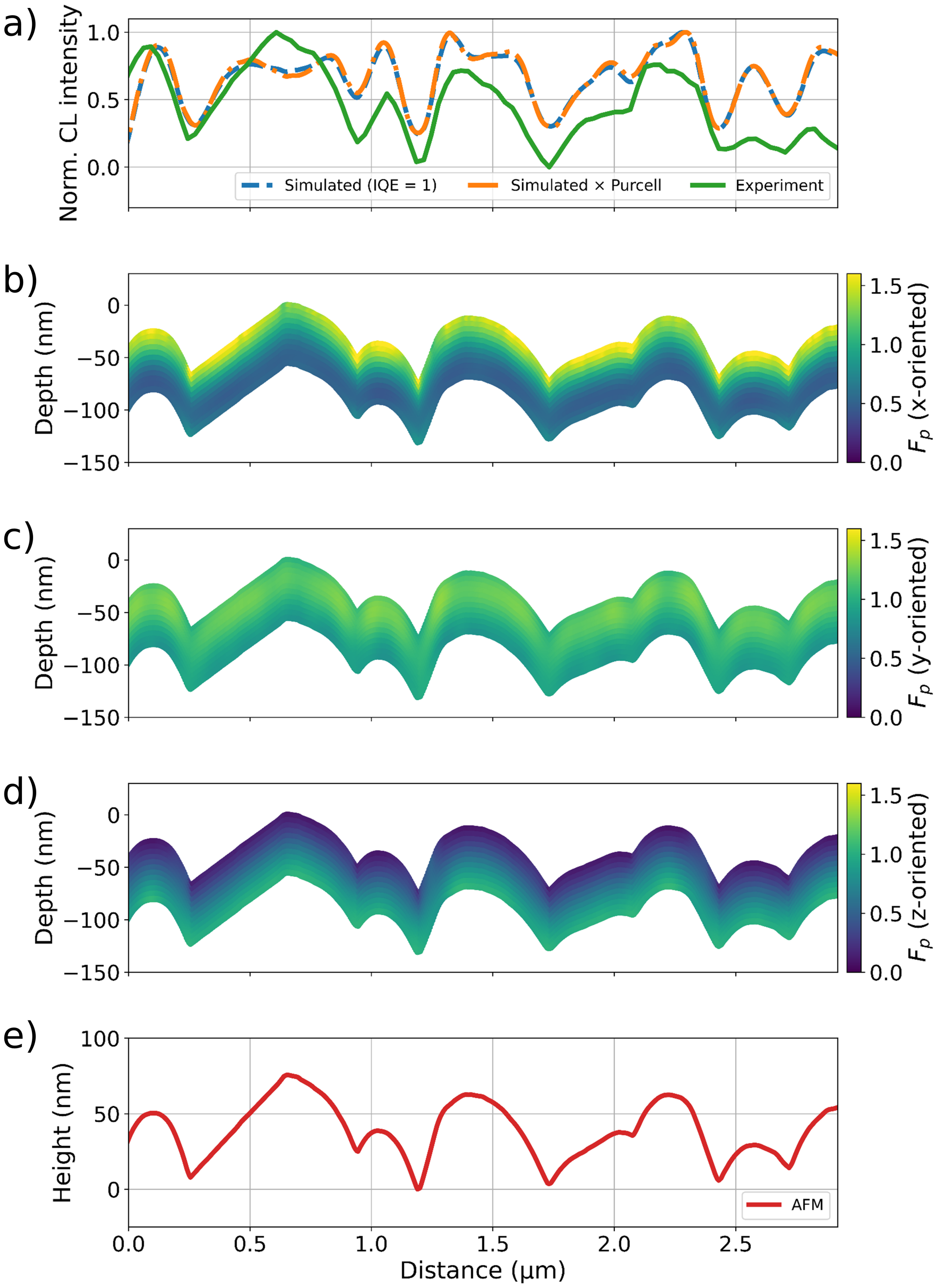

FIG. S6. (a) Experimental CL line trace (2 keV, $\lambda = 525$ nm, 6 nm bandwidth) (green) together with the simulated line traces with IQE = 1 (blue dashed line) and with IQE $\ll 1$ (dashed orange line). (b,c,d) Simulated Purcell factors as a function of position for the same geometry as in Figure 3 (b) in the main text. (e) AFM line trace that was used as an input in the simulations.

S6. LUMINESCENCE LIFETIMES

Primarily, we performed lifetime measurements to assess the degree of degradation induced by electron-beam irradiation. We find that the photoluminescence (PL) lifetime of regions exposed to the electron beam is of the same order of magnitude as that of non-irradiated areas, indicating no significant beam-induced degradation. In addition, time-resolved cathodoluminescence (TR-CL) measurements were carried out to compare luminescence lifetimes under optical and electron excitation. Whereas the dominant PL lifetime is on the order of 1–2 ns, the CL lifetime is limited by the temporal resolution of the detector ($\approx$ 50 ps).

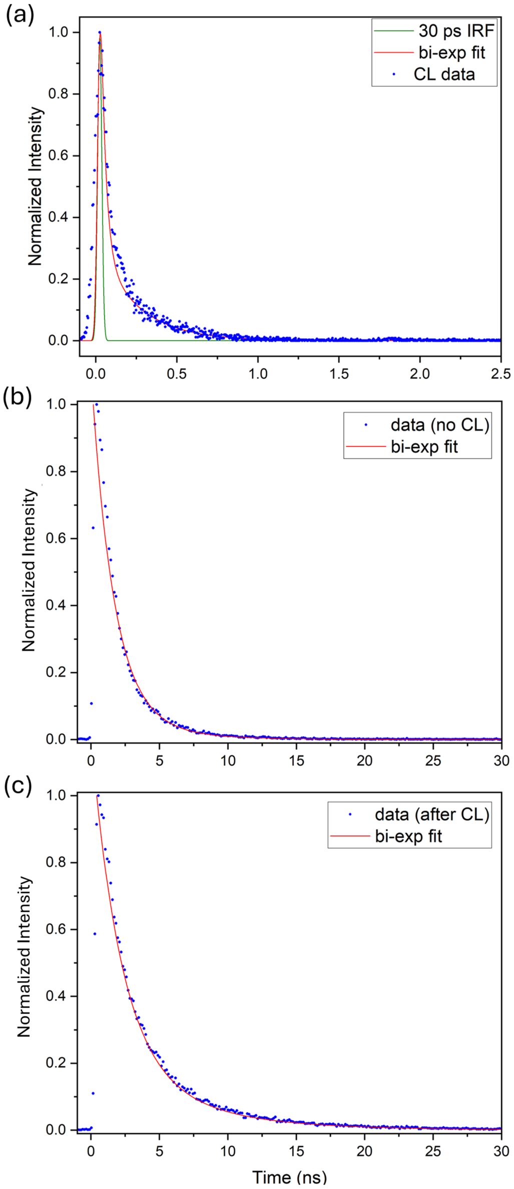

FIG. S7. (a) Time-resolved CL data (blue dots) of perovskite film with a calculated Gaussian IRF (green line) of 30 ps corresponding to the electron pulse duration of 30 ps. Bi-exponential fit (red line) with τ_1= (0.03 ± 0.01) ns and with τ_2 = (0.25 ± 0.04) ns with A_1 = (0.82 ± 0.03). (b) Time-resolved PL data (blue dot) of perovskite film before electron irradiation. Bi-exponential fit (red line) with τ_1 = (1.6 ± 0.2) ns and with τ_2 = (4.5 ± 0.6) ns with A_1 = (0.93 ± 0.03). (c) Time-resolved PL data (blue dots) of perovskite film after electron irradiation. Bi-exponential fit (red line) with τ_1 = (2.2 ± 0.1) ns and with τ_2 = (6.6 ± 0.2) ns with A_1 = (0.86 ± 0.05), confirming that the electron irradiation of the sample did not result in a shortening of the dominating lifetime component (τ_1).

The decay curves were fitted using the bi-exponential model

$$I(t) = A_1 e^{-\frac{t}{\tau_1}} + A_2 e^{-\frac{t}{\tau_2}} \tag{5}$$

weighted by amplitudes A_i, yielding two characteristic lifetimes. In both laser- and electron-excited measurements, the shorter lifetime component is dominant. From the bi-exponential fits to the CL decay curves, we extract an effective CL lifetime of 34 ps. Since the temporal resolution of the detector is specified to be larger than 50 ps, we conservatively use 50 ps as an upper bound for the effective CL lifetime. Combining this value with the previously reported diffusion coefficient for the large-grain $CsPbBr_3$ (D = 0.39 cm^2 s^{-1} [8]), we estimate an upper limit for the carrier diffusion length of ≈ 27 nm. This indicates that charge carriers generated by the incoming electron beam are predominantly confined within the electron-cascade region, and that long-range diffusion can be neglected.

S7. CATHODOLUMINESCENCE OF DIPOLE EMITTERS INSIDE A THIN PLANAR FILM

To compute the energy density of radiation emitted by a set of dipoles inside a thin film, we follow a similar procedure as outlined in the supplementary material of Ref. [9]. First, we assume a dipole placed at a fixed position inside the film, accounting for the multiple internal reflections and transmission. In a second step, we derive the associated far-field and compute the fractional light emitted in the upper half-plane.

A. Near-field of a dipole inside a slab

Let us assume a slab with permittivity ϵ_2 and thickness d, defined from $z = 0$ to $z = d$, and placed on a substrate with permittivity ϵ_3, as illustrated in Fig. S8. The space above the film is defined by ϵ_1, which in general can be different from vacuum ($\epsilon \neq 1$). The electric field created by an excited dipole $\mathbf{p}$ hosted inside the thin slab of ϵ_2 is given by [10, 11]

$$\mathbf{E}^{\rm dip} = \frac{1}{\epsilon_2}\left(k_2^2 + \nabla\times\nabla\right)\mathbf{p}\frac{\mathrm{e}^{\mathrm{i}k_2|\mathbf{r}-\mathbf{r}_0|}}{|\mathbf{r}-\mathbf{r}_0|}, \tag{6}$$

with $k = \omega/c$, $k_2 = k\sqrt{\epsilon_2}$, $\mathbf{r}_0 = (\mathbf{R}_0, z_0)$ is the position of the emitting dipole inside the thin slab, and $\mathbf{R}_0 = (x_0, y_0)$. Using Weyl's identity

$$\frac{\mathrm{e}^{\mathrm{i}k_2|\mathbf{r}-\mathbf{r}_0|}}{|\mathbf{r}-\mathbf{r}_0|} = \int \frac{d^2\mathbf{Q}}{(2\pi)^2}\frac{2\pi\mathrm{i}}{k_{2z}}\mathrm{e}^{\mathrm{i}\mathbf{Q}\cdot(\mathbf{R}-\mathbf{R}_0)}\mathrm{e}^{\mathrm{i}k_{2z}|z-z_0|}, \tag{7}$$

in which $\mathbf{Q} = (Q_x, Q_y)$ and $k_{2z} = \sqrt{k_2^2 - Q^2}$ (with $\mathrm{Im}\{k_{2z}\} > 0$), we then rewrite the electric field produced by a dipole inside a homogeneous medium as

$$\mathbf{E}^{\rm dip} = \frac{\mathrm{i}}{2\pi\epsilon_2}\int\frac{d^2\mathbf{Q}}{k_{2z}}\left[k_2^2\mathbf{p} - (\mathbf{p}\cdot\mathbf{k}_2^{\pm})\mathbf{k}_2^{\pm}\right]\mathrm{e}^{\mathrm{i}\mathbf{Q}\cdot(\mathbf{R}-\mathbf{R}_0)}\mathrm{e}^{\mathrm{i}k_{2z}|z-z_0|}, \tag{8}$$

with "+" sign for $z > z_0$ and "−" when $z < z_0$, and $k_2^{\pm} = \mathbf{Q} \pm k_{2z}\hat{z}$. Note that the unit vector $\hat{\mathbf{k}}_2^{\pm} = \mathbf{k}_2^{\pm}/k_2$ in combination with $\mathbf{e}_s = (-Q_y\hat{x} + Q_x\hat{y})/Q$ and $\mathbf{e}_{p,2}^{\pm} = (\pm k_{2z}\mathbf{Q} - Q^2\hat{z})/(Qk_2)$ form a complete set of orthonormal vectors, and therefore, we can write

$$\mathbf{E}^{\rm dip} = \frac{\mathrm{i}k^2}{2\pi}\int\frac{d^2\mathbf{Q}}{k_{2z}}\left[(\mathbf{e}_s\cdot\mathbf{p})\mathbf{e}_s + (\mathbf{e}_{p,2}^{\pm}\cdot\mathbf{p})\mathbf{e}_{p,2}^{\pm}\right]\mathrm{e}^{\mathrm{i}\mathbf{Q}\cdot(\mathbf{R}-\mathbf{R}_0)+\mathrm{i}k_{2z}|z-z_0|}. \tag{9}$$

The field above the thin film ($z > d$) is the result of the electric field produced by the dipole at the position $z = z_0$ that undergoes multiple reflections inside the thin slab (i.e., like Fabry-Pérot). Thus, the resulting electric field yields

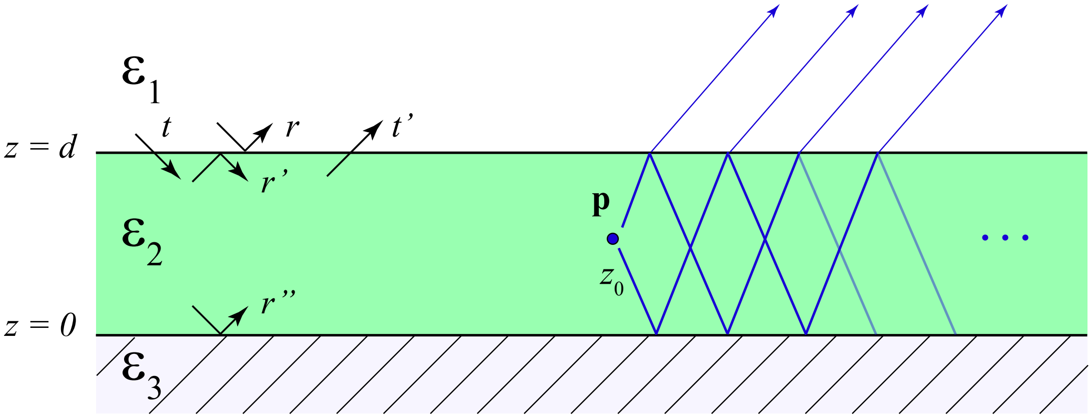

FIG. S8. **Illustration of a dipole p emitting inside a film**. A dipole radiating to the far field is placed at $z = z_0$ inside a film of thickness d and permittivity ϵ_2 supported by a substrate of permittivity ϵ_3 and covered by cladding at the upper space defined by ϵ_1. The emitted waves up- and downwards originated by the dipole suffer multiple reflections before they escape to the far field, which is described by the corresponding reflection and transmission coefficients.

$$\mathbf{E}^{\mathrm{dip}}=\frac{\mathrm{i}k^2}{2\pi}\int\frac{d^2\mathbf{Q}}{k_{2z}}\mathrm{e}^{\mathrm{i}\mathbf{Q}\cdot(\mathbf{R}-\mathbf{R}_0)+\mathrm{i}k_z(z-d)}\left\{\begin{array}{c}\mathbf{e}^{+}_{p,1}\left[(\mathbf{e}^{+}_{p,2}\cdot\mathbf{p})\dfrac{t'_{\mathrm{p}}\mathrm{e}^{\mathrm{i}k_{2z}(d-z_0)}}{1-r'_{\mathrm{p}}r''_{\mathrm{p}}\mathrm{e}^{2\mathrm{i}k_{2z}d}}+(\mathbf{e}^{-}_{p,2}\cdot\mathbf{p})\dfrac{r''_{\mathrm{p}}t'_{\mathrm{p}}\mathrm{e}^{\mathrm{i}k_{2z}(d+z_0)}}{1-r'_{\mathrm{p}}r''_{\mathrm{p}}\mathrm{e}^{2\mathrm{i}k_{2z}d}}\right]\\ +\mathbf{e}_s(\mathbf{e}_s\cdot\mathbf{p})\dfrac{t'_{\mathrm{s}}}{1-r'_{\mathrm{s}}r''_{\mathrm{s}}\mathrm{e}^{\mathrm{i}2k_{2z}d}}\left[\mathrm{e}^{\mathrm{i}k_{2z}(d-z_0)}+r''_{\mathrm{s}}\,\mathrm{e}^{\mathrm{i}k_{2z}(d+z_0)}\right]\end{array}\right\}, \tag{10}$$

where we have that the light waves have reflected multiple times inside the thin film and have already transmitted to medium 1 (i.e., right above the film). We use the well-known Fresnel coefficients [11, 12] for planar interfaces that describe how light scatters when going from medium 1 to medium 2, which are defined as

$$r_{\mathrm{s},12}=\frac{k_{z1}-k_{z2}}{k_{z1}+k_{z2}},\qquad t_{\mathrm{s},12}=\frac{2k_{z1}}{k_{z1}+k_{z2}}, \tag{11}$$

$$r_{\mathrm{p},12}=\frac{\epsilon_2k_{z1}-\epsilon_1k_{z2}}{\epsilon_2k_{z1}+\epsilon_1k_{z2}},\qquad t_{\mathrm{p},12}=\frac{2\sqrt{\epsilon_1\epsilon_2}k_{z1}}{\epsilon_2k_{z1}+\epsilon_1k_{z2}}, \tag{12}$$

and in particular, we used

$$r'_{\mathrm{s}}=\frac{k_{2z}-k_{1z}}{k_{2z}+k_{1z}},\qquad r''_{\mathrm{s}}=\frac{k_{2z}-k_{3z}}{k_{2z}+k_{3z}},\qquad t'_{\mathrm{s}}=\frac{2k_{2z}}{k_{2z}+k_{1z}}, \tag{13}$$

$$r'_{\mathrm{p}}=\frac{\epsilon_1k_{2z}-\epsilon_2k_{1z}}{\epsilon_1k_{2z}+\epsilon_2k_{1z}},\qquad r''_{\mathrm{p}}=\frac{\epsilon_3k_{2z}-\epsilon_2k_{3z}}{\epsilon_3k_{2z}+\epsilon_2k_{3z}},\qquad t'_{\mathrm{p}}=\frac{2\sqrt{\epsilon_2\epsilon_1}k_{2z}}{\epsilon_1k_{2z}+\epsilon_2k_{1z}}. \tag{14}$$

B. Calculation of the fractional energy radiated into the far-field

Let us define as Γ_{CL} the angle-integrated Poynting vector $\mathbf{S}$ in the upper half plane (i.e., $\Omega>0$) in the far-field per unit of frequency as

$$\Gamma_{\mathrm{CL}}(\omega,z_0)=\frac{r^2}{\hbar\omega}\int_{\Omega>0}d\Omega\,\langle\hat{r}\cdot\mathbf{S}\rangle_{\mathrm{time}}=\frac{1}{2\pi\hbar k}\int_0^{\pi/2}\sin\theta\,d\theta\int_0^{2\pi}d\varphi\,|\mathbf{f}(\hat{r},z_0)|^2. \tag{15}$$

In particular, the radiated energy is given by the resulting Poynting vector $\mathbf{S}=(c/4\pi)(\mathbf{E}^{\mathrm{FF}}+\mathrm{c.c.})\times(\mathbf{H}^{\mathrm{FF}}+\mathrm{c.c.})$, with the magnetic field obtained from Faraday's law $\mathbf{H}^{\mathrm{FF}}=-(\mathrm{i}/k)\nabla\times\mathbf{E}^{\mathrm{FF}}$, and the electric field defined in the far-field as $\mathbf{E}^{\mathrm{FF}}=\mathbf{f}(\hat{r},z_0)\mathrm{e}^{\mathrm{i}kr}/r$. Note that we assume a temporal dependence $\mathrm{e}^{-\mathrm{i}\omega t}$ in the magnetic and electric fields, which yields a factor of 1/2 when performing the time average (i.e., $T^{-1}\int_0^T dt\sin^2(\omega t)=1/2$).
To obtain the expression of $\mathbf{f}(\hat{r},z_0)$, we note that in the far-field, we take the limit of $kr\to\infty$, such that the integral in $\mathbf{Q}$ gives rise to the following type

$$\lim_{kr\to\infty}\int\frac{d^2\mathbf{Q}}{(2\pi)^2}\mathrm{e}^{\mathrm{i}\mathbf{k}\cdot\mathbf{r}}\mathbf{g}(\mathbf{Q})=\frac{k_z}{2\pi\mathrm{i}}\mathbf{g}(\mathbf{Q}_0)\frac{\mathrm{e}^{\mathrm{i}kr}}{r}, \tag{16}$$

with $\mathbf{Q}_0=(\mathbf{R}/r)k$, whose solution is found by using the stationary phase approximation (see the equation above Eq. 8.53 in Ref. [11]). Thereby, the amplitude of the electric far-field in Eq. (10) reads

$$\mathbf{f}(\hat{r},z_0)=\mathrm{e}^{-\mathrm{i}(\mathbf{Q}_0\cdot\mathbf{R}_0+k_zd)}\frac{k^2k_z}{k_{2z}}\left\{\begin{array}{c}\mathbf{e}^{+}_{p,1}\left[(\mathbf{e}^{+}_{p,2}\cdot\mathbf{p})\dfrac{t'_{\mathrm{p}}\mathrm{e}^{\mathrm{i}k_{2z}(d-z_0)}}{1-r'_{\mathrm{p}}r''_{\mathrm{p}}\mathrm{e}^{2\mathrm{i}k_{2z}d}}+(\mathbf{e}^{-}_{p,2}\cdot\mathbf{p})\dfrac{r''_{\mathrm{p}}t'_{\mathrm{p}}\mathrm{e}^{\mathrm{i}k_{2z}(d+z_0)}}{1-r'_{\mathrm{p}}r''_{\mathrm{p}}\mathrm{e}^{2\mathrm{i}k_{2z}d}}\right]\\ +\mathbf{e}_s(\mathbf{e}_s\cdot\mathbf{p})\dfrac{t'_{\mathrm{s}}}{1-r'_{\mathrm{s}}r''_{\mathrm{s}}\mathrm{e}^{\mathrm{i}2k_{2z}d}}\left[\mathrm{e}^{\mathrm{i}k_{2z}(d-z_0)}+r''_{\mathrm{s}}\,\mathrm{e}^{\mathrm{i}k_{2z}(d+z_0)}\right]\end{array}\right\}, \tag{17}$$

where, we note that $\mathbf{k}=(\mathbf{Q}_0,k_z)=k\hat{r}$, $\mathbf{Q}_0=k\,(\mathbf{R}/r)=k(\hat{x}\cos\varphi+\hat{y}\sin\varphi)\sin\theta$, and $k_z=k\,(z/r)=k\cos\theta$. Moreover, in the calculation of $|\mathbf{f}(\hat{r},z_0)|^2$, we obtain

$$|\mathbf{f}(\hat{r},z_0)|^2=\left|\frac{k^2k_z}{k_{2z}}\right|^2\left\{\begin{array}{c}\left|\dfrac{t'_{\mathrm{p}}}{1-r'_{\mathrm{p}}r''_{\mathrm{p}}\mathrm{e}^{2\mathrm{i}k_{2z}d}}\left[(\mathbf{e}^{+}_{p,2}\cdot\mathbf{p})\mathrm{e}^{\mathrm{i}k_{2z}(d-z_0)}+(\mathbf{e}^{-}_{p,2}\cdot\mathbf{p})r''_{\mathrm{p}}\mathrm{e}^{\mathrm{i}k_{2z}(d+z_0)}\right]\right|^2\\ +\left|(\mathbf{e}_s\cdot\mathbf{p})\dfrac{t'_{\mathrm{s}}}{1-r'_{\mathrm{s}}r''_{\mathrm{s}}\mathrm{e}^{\mathrm{i}2k_2d}}\left[\mathrm{e}^{\mathrm{i}k_2(d-z_0)}+r''_{\mathrm{s}}\,\mathrm{e}^{\mathrm{i}k_2(d+z_0)}\right]\right|^2\end{array}\right\}. \tag{18}$$

To compute the angular integrals in Eq. (15), we project the emission direction of the dipole so that

$$\mathbf{e}_s \cdot \hat{z} p_z = 0, \qquad \mathbf{e}^{\pm}_{p,2} \cdot \hat{z} p_z = \frac{-Q}{k_2} p_z, \tag{19}$$

$$\mathbf{e}_s \cdot \hat{x} p_x = \frac{-Q_y}{Q} p_x, \qquad \mathbf{e}^{\pm}_{p,2} \cdot \hat{x} p_x = \pm \frac{Q_x k_{2z}}{Q k_2} p_x, \tag{20}$$

$$\mathbf{e}_s \cdot \hat{y} p_y = \frac{Q_x}{Q} p_y, \qquad \mathbf{e}^{\pm}_{p,2} \cdot \hat{y} p_y = \pm \frac{Q_y k_{2z}}{Q k_2} p_y. \tag{21}$$

and solve for the polar angle $d\varphi$ integral, following the results

$$\int_0^{2\pi} d\varphi \left(\frac{Q_x}{Q}\right)^2 = \int_0^{2\pi} d\varphi \left(\frac{Q_y}{Q}\right)^2 = \pi, \tag{22}$$

$$\int_0^{2\pi} d\varphi \, \frac{Q_x Q_y}{Q^2} = \int_0^{2\pi} d\varphi \, Q_x = \int_0^{2\pi} d\varphi \, Q_y = 0, \tag{23}$$

$$\int_0^{2\pi} d\varphi = 2\pi. \tag{24}$$

After solving the above integrals, we note that the dipole emission direction can be treated independently after integrating over the azimuthal angle. Then, we write Eq. (15) for the rate of emitted photons as

$$\Gamma(\omega, z_0) = \int_0^{\pi/2} \sin\theta \, d\theta \left[(|p_x|^2 + |p_y|^2) G_{\parallel}(\theta) + |p_z|^2 G_{\perp}(\theta) \right]. \tag{25}$$

We assume all dipoles to have the same strength $|p_x|^2 = |p_y|^2 = |p_z|^2 \equiv |p(z_0)|^2$, thereby,

$$\Gamma_{\mathrm{CL}}(\omega, z_0) = |p|^2 \int_0^{\pi/2} \sin\theta \, d\theta \left[2G_{\parallel}(\theta) + G_{\perp}(\theta) \right], \tag{26}$$

where the integral can be limited to the numerical aperture (NA) of the objective if needed (here not used, see more information about it in Ref. [10]). We define the $G_{\parallel}$ and $G_{\perp}$ functions as

$$G_{\parallel}(\theta) = \frac{\pi}{2\pi\hbar k} \left| \frac{k_z k^2}{k_{2z}} \right|^2 \left\{ \begin{array}{l} \left| \dfrac{k_{2z}}{k_2} \right|^2 \left| \dfrac{t'_{\mathrm{p}}}{1 - r'_{\mathrm{p}} r''_{\mathrm{p}} \mathrm{e}^{2\mathrm{i}k_{2z}d}} \left[\mathrm{e}^{\mathrm{i}k_{2z}(d-z_0)} - r''_{\mathrm{p}} \mathrm{e}^{\mathrm{i}k_{2z}(d+z_0)} \right] \right|^2 \\ + \left| \dfrac{t'_{\mathrm{s}}}{1 - r'_{\mathrm{s}} r''_{\mathrm{s}} \mathrm{e}^{2\mathrm{i}k_{2z}d}} \left[\mathrm{e}^{\mathrm{i}k_{2z}(d-z_0)} + r''_{\mathrm{s}} \mathrm{e}^{\mathrm{i}k_{2z}(d+z_0)} \right] \right|^2 \end{array} \right\} \tag{27}$$

$$G_{\perp}(\theta) = \frac{2\pi}{2\pi\hbar k} \left| \frac{k_z k^2}{k_{2z}} \right|^2 \left\{ \left| \frac{Q_0}{k_2} \right|^2 \left| \frac{t'_{\mathrm{p}}}{1 - r'_{\mathrm{p}} r''_{\mathrm{p}} \mathrm{e}^{2\mathrm{i}k_{2z}d}} \left[\mathrm{e}^{\mathrm{i}k_{2z}(d-z_0)} + r''_{\mathrm{p}} \mathrm{e}^{\mathrm{i}k_{2z}(d+z_0)} \right] \right|^2 \right\}, \tag{28}$$

which play a similar role to Green's functions. Remember that $Q_0 = k \sin\theta$ and $k_{jz}^2 = k_j^2 - Q_0^2$ with $k_j = (\omega/c)\sqrt{\epsilon_j}$.

C. Cathodoluminescence intensity

The measured Cathodoluminescence intensity (CL) is given by the integration of $\Gamma_{\mathrm{CL}}(\omega, z_0)$ over all dipole positions. However, as discussed in the main text, we weight the dipole distribution by the excitation density calculated using Monte Carlo simulations. Thereby, we assume that $|\mathbf{E}^{\mathrm{ext}}(z_0)| \propto P(z_0)$, where $P(z_0)$ is the average probability of the energy deposited by the electron as a function of z_0.

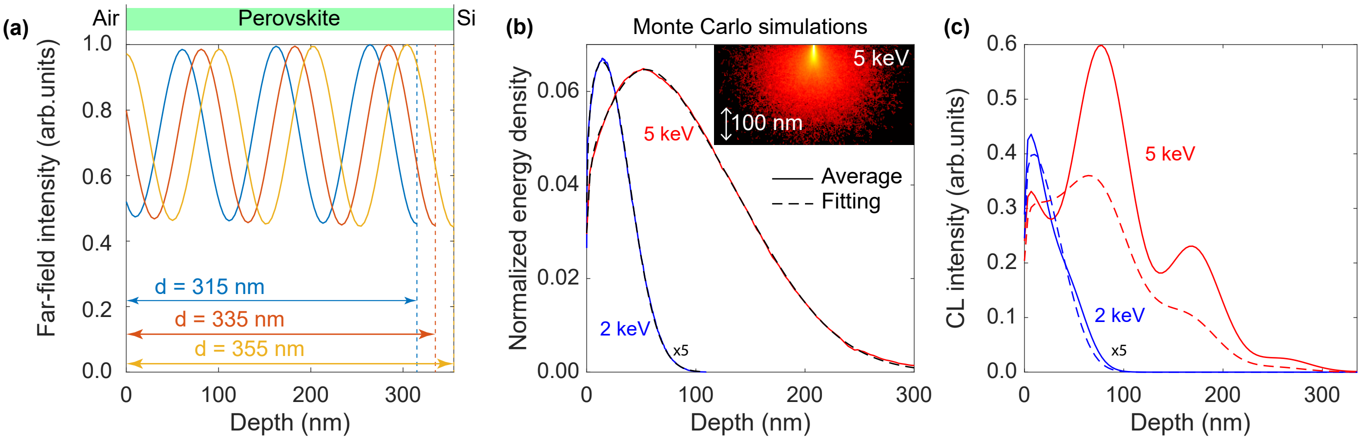

FIG. S9. **Cathodoluminescence from a thin film.** (a) Normalized far-field intensity of an excited dipole placed at z_0 inside a perovskite film with refractive index 2.67 at 525 nm wavelength [13]. Results are normalized to the maximum intensity for different thickness d (see different colors) and computed using Eq. (25). The film is deposited on top of silicon (Si) with a refractive index of 4.18 [14], and surrounded by air (i.e., $\epsilon = 1$). (b) Averaged energy density deposited using Monte Carlo simulations in one dimension (see inset for a two-dimensional representation) by a 2-keV electron (blue solid curve) and 5-keV electron (red curve), computed using Eq. (30). Dashed lines are Gaussian fittings according to Eq. (31). (c) Resulting CL emission computed from the product of the dipole far-field emission intensity in (a) for a 335-nm thick perovskite film and the corresponding excitation profile in (b) of 2 (blue curve) and 5 keV (red) electrons. Dashed curves show the same for a lossy perovskite using $\epsilon = (2.67 + 0.1562\mathrm{i})^2$ [13].

In Fig. S9a, we show the calculated radiated emission intensity of a dipole into the far-field placed at position z_0 inside the sketched layered structure, in arbitrary units given by Eq. (25). Different colored lines indicate the emission profile for different film thicknesses (see labels). Panel Fig. S9b describes the laterally average excitation density of the electron cascade as a function of depth as described in Sec. S7 C 1 below, for 2 and 5 kV acceleration voltages (blue and red curves, respectively). Figure S9c shows the resulting CL intensity $\Gamma_{\rm CL}(\omega)$ obtained from the multiplication of the dipole emission intensity (panel Fig. S9a) with the excitation profile (panel Fig. S9b). Additionally, we compute the normalized values of $\Gamma_{\rm CL}(\omega)$ in Fig. S10a as

$$\Gamma_{\rm CL}(\omega) = \int dz_0\, \Gamma_{\rm CL}(\omega, z_0) P(z_0), \tag{29}$$

for two different acceleration voltages and as a function of the film thickness, with damping (solid curves) and without (dashed curves). Interestingly, we observe that for the lower acceleration voltages (2 keV electrons, blue curve), the intensity varies more than at higher acceleration voltages (5 keV electrons, red curve). To quantify the contrast of the fringes, we define in Fig. S10b their visibility, respectively, showing that CL images from 2-keV electrons have a twofold resolution compared to the 5-keV ones. Note that introducing loss to the perovskite optical constant shifts the curves due to changes in the interference condition.

1. *Fitting of energy density deposition from Monte Carlo simulations*

In order to extract an effective one-dimensional energy density deposition from the three-dimensional Monte Carlo simulations $E_{\rm MC}$, we average all the probabilities through the depth of the film such that

$$P_{\rm MC}(z) = \frac{\sum_{i,j} E_{\rm MC}(x_i, y_j, z)}{\sum_{i,j} \Delta x_i \Delta y_i}, \tag{30}$$

where $\Delta x_i \Delta y_i$ is the surface element. We process the data by fitting the resulting $P_{\rm MC}(z)$ for 2 and 5 keV acceleration voltages to

$$P_{\rm fitting}(z) = \sum_{i=1}^{3} a_i \mathrm{e}^{-(z-b_i)^2/c_i^2}, \tag{31}$$

where the gaussian coefficients are in table S1.

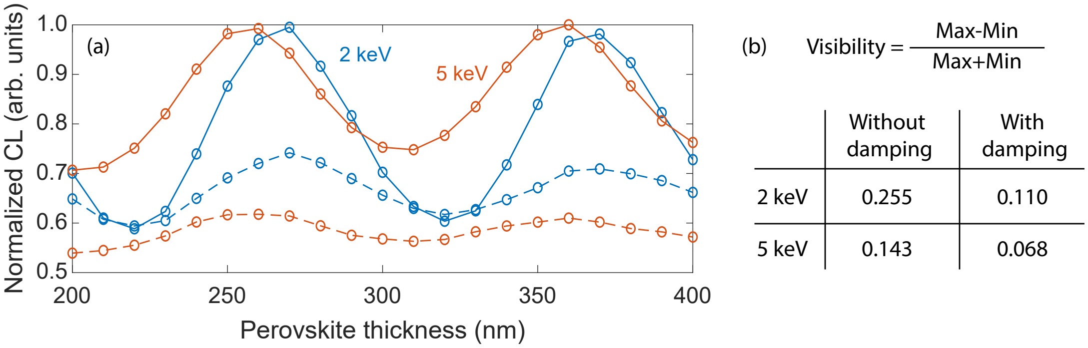

	Without damping	With damping
2 keV	0.255	0.110
5 keV	0.143	0.068

FIG. S10. **Normalized cathodoluminescence in a perovskite film.** (a) We show the normalized angle-integrated CL spectra for different perovskite film thicknesses at 2 keV (blue curve) and 5 keV (red) electrons, accounting for their electron cascade density and obtained from Eq. (29). Dashed curves simulate a lossy perovskite using $\epsilon = (2.67 + 0.1562\mathrm{i})^2$. (b) Calculation of the visibility using the definition given in the inset for all cases in (a).

TABLE S1. Gaussian fit coefficients for 2 kV and 5 kV acceleration voltages.

Voltage	a_1	b_1	c_1	a_2	b_2	c_2	a_3	b_3	c_3
2 kV	1.168×10^{-4}	13.02	1.368	0.01325	14.49	35.61	-3.514×10^{5}	-69.2	16.18
5 kV	0.01616	36.2	56.97	0.05166	74.24	112.7	-1.202×10^{10}	-132.8	25.34

D. Centroid of the dominant emission

In order to quantify at which effective depth the maximum of the emission is occurring for a given film thickness, we can compute the centroid of the emitted CL by computing

$$\text{Penetration depth centroid} = \frac{\int z_0 dz_0 \, \Gamma_{\mathrm{CL}}(\omega, z_0) P(z_0)}{\int dz_0 \, \Gamma_{\mathrm{CL}}(\omega, z_0) P(z_0)}, \tag{32}$$

which we show in Fig. S11 for different electron kinetic energies as a function of the perovskite thickness. We can see that the 2 keV electrons (blue curve) excite CL more effectively at a depth of 20-30 nm, depending on the thickness, while higher-energy electrons with 5 keV kinetic energy (red curve) most effectively excite CL at 90-95 nm depth. The values are calculated using 525 nm wavelength (~ 2.36 eV), and while the damping does not play a major role for 2 keV electrons (dashed curves), in the case of the 5 keV electrons, the centroid drops to values around ~ 80 nm.

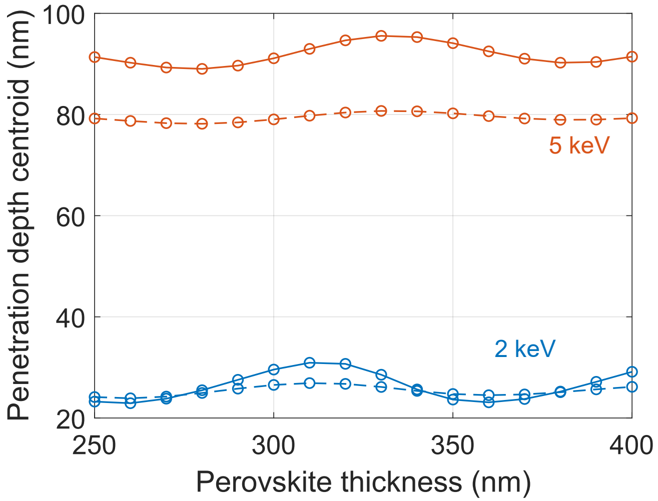

FIG. S11. **Centroid of the normalized cathodoluminescence from perovskite.** We show the centroid of the normalized integrated CL spectra for different perovskite thicknesses for 2 keV (blue curve) and 5 keV (red) electrons at 525 nm light wavelength. Solid lines do not include damping where $\epsilon = 2.67^2$, while dashed ones model the perovskite with the corresponding attenuation coefficient in which $\epsilon = (2.67 + 0.1562\mathrm{i})^2$.

[1] C. A. Rico-Yuson, S. Danwittayakul, S. Kumar, G. L. Hornyak, and T. Bora, Sequential dip-coating of CsPbBr3 perovskite films in ambient conditions and their photovoltaic performance, Journal of Materials Science **57**, 10285 (2022).

[2] S. M. Qaid, H. M. Ghaithan, B. A. Al-Asbahi, and A. S. Aldwayyan, Ultra-stable polycrystalline CsPbBr3 perovskite–polymer composite thin disk for light-emitting applications, Nanomaterials **10**, 1 (2020).

[3] I. Dursun, M. De Bastiani, B. Turedi, B. Alamer, A. Shkurenko, J. Yin, A. M. El-Zohry, I. Gereige, A. AlSaggaf, O. F. Mohammed, M. Eddaoudi, and O. M. Bakr, CsPb2Br5 Single Crystals: Synthesis and Characterization, ChemSusChem **10**, 3746 (2017).

[4] K. Drexhage, Influence of a dielectric interface on fluorescence decay time, Journal of Luminescence **1-2**, 693 (1970).

[5] E. Snoeks, A. Lagendijk, and A. Polman, Measuring and modifying the spontaneous emission rate of erbium near an interface, Phys. Rev. Lett. **74**, 2459 (1995).

[6] R. J. Walters, J. Kalkman, A. Polman, H. A. Atwater, and M. J. A. de Dood, Photoluminescence quantum efficiency of dense silicon nanocrystal ensembles in Sio_2, Phys. Rev. B **73**, 132302 (2006).

[7] J. Kalkman, H. Gersen, L. Kuipers, and A. Polman, Excitation of surface plasmons at a $\mathrm{Sio}_2\mathrm{Ag}$ interface by silicon quantum dots: Experiment and theory, Phys. Rev. B **73**, 075317 (2006).

[8] Y. Lu, Y. K. Jung, M. Dubajic, X. Li, S. Maqbool, Q. Gu, X. Bai, Y. Boeije, X. W. Chua, A. J. Mirabelli, T. Kang, L. Sonneveld, Y. Zhang, T. A. Selby, C. Mamak, K. Tang, Z. Yu, T. Liu, M. Anaya, S. Barlow, S. R. Marder, B. Ehrler, C. Ducati, R. H. Friend, and S. D. Stranks, Layer-by-layer epitaxial growth of perovskite heterostructures with tunable band offsets, Science **390**, 716 (2025).

[9] A. R. Bowman, A. Rodríguez Echarri, F. Kiani, F. Iyikanat, T. V. Tsoulos, J. D. Cox, R. Sundararaman, F. J. García de Abajo, and G. Tagliabue, Quantum-mechanical effects in photoluminescence from thin crystalline gold films, Light: Science & Applications **13**, 91 (2024).

[10] L. Novotny and B. Hecht, *Principles of Nano-optics* (Cambridge University Press, New York, 2006).

[11] U. Hohenester, *Nano and quantum optics: an introduction to basic principles and theory* (Springer Nature, 2019).

[12] J. D. Jackson, *Classical Electrodynamics* (Wiley, New York, 1999).

[13] G. Ermolaev, A. P. Pushkarev, A. Zhizhchenko, A. A. Kuchmizhak, I. Iorsh, I. Kruglov, A. Mazitov, A. Ishteev, K. Konstantinova, D. Saranin, A. Slavich, D. Stosic, E. S. Zhukova, G. Tselikov, A. Di Carlo, A. Arsenin, K. S. Novoselov, S. V. Makarov, and V. S. Volkov, Giant and tunable excitonic optical anisotropy in single-crystal halide perovskites, Nano Letters **23**, 2570 (2023), pMID: 36920328, https://doi.org/10.1021/acs.nanolett.2c04792.

[14] E. D. Palik, *Handbook of optical constants of solids*, Vol. 3 (Academic press, 1998).